PAPER

Check for updates

Electrokinetic flow instabilities in shear thinning fluids with conductivity gradients

To-Lin Chen, [ID] [ab] Mahmud Kamal Raihan, [ID] [b] Seyed Mojtaba Tabarhoseini, [b] Chase T. Gabbard, [b] Md Mainul Islam, [b] Yu-Hsiang Lee, [b] Joshua B. Bostwick, [ID] [b] Lung-Ming Fu [ID] *[a] and Xiangchun Xuan [ID] *[b]

Instabilities in the form of periodic or irregular waves at the fluid interface have been demonstrated in microchannel electrokinetic flows with conductivity gradients when the applied electric field is above a threshold value. Most prior studies on electrokinetic instabilities (EKI) are restricted to Newtonian fluids though many of the chemical and biological samples in microfluidic applications exhibit non-Newtonian characteristics. We present in this work an experimental study of the effects of fluid shear thinning on the development of EKI waves through the addition of a small amount of xanthan gum (XG) polymer to both the high- and low-concentration Newtonian buffer solutions. The threshold electric field for the onset of EKI in the XG solution is significantly lower than in the Newtonian solution. However, the propagation speed, amplitude and frequency of EKI waves in the former are all smaller. Increasing the polymer concentration reduces the threshold electric field and as well the critical electric Rayleigh number that considers the fluid property variations in XG solutions. This decreasing trend indicates the enhancing effect of fluid shear thinning on EKI, which is qualitatively consistent with a recent numerical prediction. However, the measured wave properties all follow a non-monotonic trend with XG concentration, different from the continuously decreasing electroosmotic velocity.

1. Introduction

Electrokinetic flow is an effective means to pump and manipulate samples in micro/nanofluidic devices.[1–3] It has a nearly plug-like velocity profile, which, compared to the parabolic pressure-driven flow, leads to a smaller flow resistance and a weaker sample dispersion.[4–6] This electric field-driven flow is, however, sensitive to both the wall (of microchannels) and fluid properties, which must be kept uniform to avoid any electric field-induced charges and in turn local flow disturbances.[7–9] Instabilities can occur in electrokinetic microchannel flows with conductivity gradients when the applied electric field is above a threshold value.[10] These so-called electrokinetic instabilities (EKI)[11] refer to the onset and growth of periodic or irregular waves at the fluid interface. On one hand, EKI must be avoided in field amplified sample stacking[12] (*e.g.*, isotachophoresis[13]) and electroosmotic flow displacement[14] (*e.g.*, electric current monitoring for an accurate measurement of electroosmotic flow velocity[15]), where two (or more) fluidic samples displacing each other have different properties with the gradient being collinear with the applied electric field.[16] EKI

should also be minimized in sheath focusing-based separation of particles,[17] where the co-flowing sheath fluid and particulate solution may have dissimilar properties with the gradient being orthogonal to the applied electric field.[18] On the other hand, EKI can be utilized to enhance the microfluidic mixing of two (or more) co-flowing samples, wherein the property gradient is also orthogonal to the applied electric field.[19–21] Understanding the mechanism of EKI is critical for proper and optimal operation of the aforementioned electrokinetic microfluidic applications.

Earlier works from the Santiago group[22–25] in 2000s established the theoretical framework of EKI in microchannel flows with conductivity gradients. Convective and absolute instabilities are identified, of which the former is convected downstream by electroosmotic flow and its onset is governed by the critical electric Rayleigh number,[23]

$$\mathrm{Ra_{e,cr}} = \Gamma \frac{h}{\delta} \frac{\varepsilon E_{th}{}^2 d^2}{\mu D} \qquad (1)$$

where $\Gamma = (\gamma - 1)^2/(\gamma + 1)^2$ with γ being the conductivity ratio between the higher and lower conductivity fluids, h is the half width of the microchannel, δ is the diffusion length of ions, ε is the fluid permittivity, E_{th} is the threshold DC electric field for the onset of EKI, d is the half depth of the microchannel, μ is the fluid viscosity, and D is the effective diffusivity of ions. The effects of

[a] *Department of Engineering Science, National Cheng Kung University, Tainan 70101, Taiwan. E-mail: loudyfu@mail.ncku.edu.tw*

[b] *Department of Mechanical Engineering, Clemson University, Clemson, SC 29634, USA. E-mail: xcxuan@clemson.edu*

various parameters, ranging from AC electric field[26,27] to fluid properties,[28–30] colloidal suspension,[31] channel structure,[32–34] channel dimension,[35,36] and Joule heating[37] have been experimentally and/or theoretically investigated on EKI in microchannel flows with conductivity and/or permittivity gradients. However, all these studies are focused upon the electrokinetic flow of Newtonian fluids.

As many of the chemical (*e.g.*, polymer solutions and colloidal suspensions) and biological (*e.g.*, blood, saliva and semen) samples in microfluidic applications are non-Newtonian fluids,[38–44] it is important to investigate the role of fluid rheology in EKI. To our knowledge, only a few studies have appeared in the literature. Our group has reported the first experimental study of EKI in viscoelastic polyethylene oxide (PEO) solution flows.[45] The addition of PEO polymer into the co-flowing Newtonian buffer solutions with different conductivities causes first a decrease then an increase in the threshold electric field for the onset of EKI. It also reduces the propagation speed and temporal frequency of EKI waves. In a later numerical work, Sasmal[46] modeled the viscoelasticity effect using the Oldroyd-B constitutive equation, which predicts suppressed EKI in viscoelastic fluid flows. Moreover, the author reported that the chaotic fluctuation of EKI decreases when the Weissenberg number or polymer-to-solvent viscosity ratio increases because of the formation of a strand of high elastic stresses at the fluid interface. In a more recent paper, Hamid and Sasmal[47] performed a numerical investigation of how the rheological behavior of a fluid obeyed by the power-law constitutive equation influences EKI. Changing the fluid rheological behavior from shear thickening to shear thinning significantly increases the intensity of EKI and decreases the threshold electric field. The authors also employed a data-driven dynamic mode decomposition technique to analyze the flow dynamics and EKI mixing. They observed a significant difference in the coherent flow structures as the power-law index changes.

Recognizing the scarcity of studies on EKI in non-Newtonian fluids, we present in this work an experimental study of EKI in shear thinning fluid flows with conductivity gradients through a T-shaped microchannel. We mix a small amount of xanthan gum (XG) polymer into high- and low-concentration Newtonian buffer solutions to form shear thinning fluids. We compare the threshold electric field for the onset of EKI waves as well as the wave speed, amplitude and frequency under different electric fields in the shear thinning and Newtonian fluid flows. We also examine how varying the XG concentration and hence the fluid shear thinning effect change the threshold electric field and the properties of EKI waves. Moreover, we revise the critical electric Rayleigh number defined in eqn (1) to incorporate the fluid property variations in XG solutions. We examine how this dimensionless number is affected by the fluid shear thinning effect and compare the result with the numerical prediction of Hamid and Sasmal.[47] The findings from this study will provide a foundation for future experimental and numerical investigations into the role of shear thinning behavior in the electroosmotic flow of more complex fluids.

2. Experiment

2.1. Materials

A similar setup to that in our previous papers on EKI in Newtonian fluid flows[29,30] was used in this experiment. The T-shaped microchannel was fabricated with polydimethylsiloxane (PDMS) using the standard soft lithography technique as detailed in our earlier paper.[29] The channel has two 8 mm long, 100 μm wide side branches and one 10 mm long, 200 μm wide main branch with a depth of 53 μm everywhere. It was primed with deionized water (Fisher Scientific) for 10 min immediately after the fabrication to ensure uniformity and reproducibility of wall properties. The inlet and outlet reservoirs of the channel were all made large with 6-mm diameter each to minimize the influence of the hydrostatic pressure-driven backflow because of the electroosmotic fluid depletion/buildup therein. The same amount of XG polymer (Tokyo Chemical Industry) was dissolved into 2 mM and 0.2 mM phosphate buffer solutions to prepare shear thinning fluids. The XG concentration was changed from 0 (*i.e.*, polymer-free
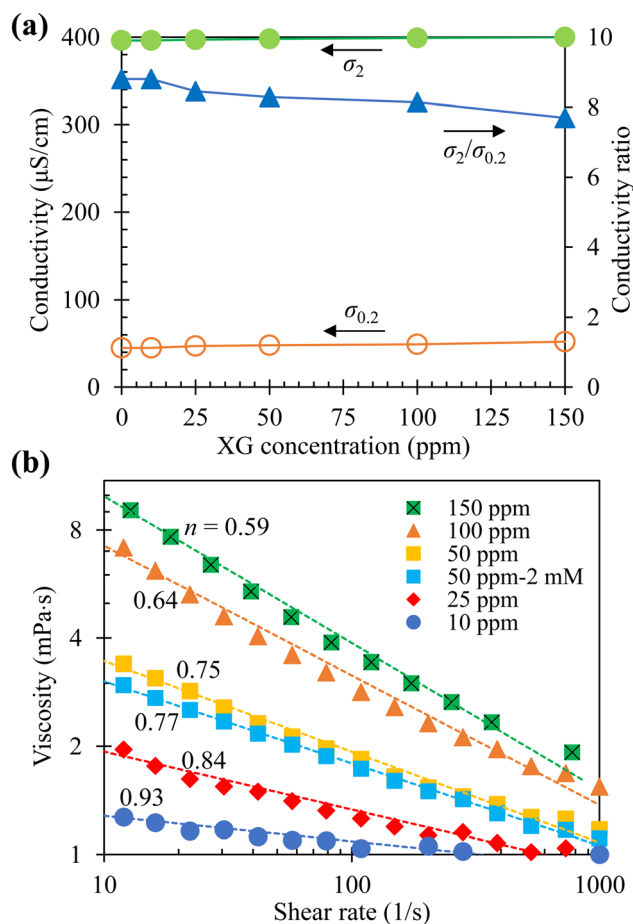

Fig. 1 Experimentally measured fluid properties: (a) electric conductivities of 2.0 mM (σ_2, filled circles) and 0.2 mM ($\sigma_{0.2}$, hollow circles) buffer-based XG solutions and the corresponding conductivity ratio (filled triangles), $\sigma_2/\sigma_{0.2}$, vs. XG concentration, where the lines are used to guide the eyes only; (b) dynamic viscosity of 0.2 mM buffer (unless otherwise stated)-based XG solutions vs. shear rate, where the power-law index, n, of the trendline fitted to the data for each solution is labeled on the log–log plot.

Newtonian fluid as the control test experiment) to 10, 25, 50, 100 and 150 ppm. These 2 mM and 0.2 mM buffer-based solutions have identical fluid properties except for the electric conductivity and wall surface charge.

The measured electric conductivities (Fisher Scientific, Accumet AP85) of the prepared fluids are presented in Fig. 1(a). Like the viscoelastic PEO solutions in our recent work,[45] the addition of a small amount of XG polymer causes no visible change in the conductivity of 2 mM buffer. It, however, slightly increases the conductivity of 0.2 mM buffer because of the small conductivity of the latter. The consequence is a decreasing conductivity ratio between 2 mM and 0.2 mM buffer-based XG solutions from 8.8 to 7.7 when the XG concentration increases from 0 to 150 ppm. The dynamic viscosity, η, of the prepared XG solutions was measured using a cone-plate rheometer (Anton Paar, MCR 302) at room temperature through steady-shear tests for shear rates ranging from 10 to 1000 s^{-1}. The cone and plate have a diameter of 50 mm, and the cone has an angle of 1°. The obtained viscosity data are shown in Fig. 1(b) with respect to the shear rate for 0.2 mM buffer-based solutions at different XG concentrations. Also included in the log–log plot is the viscosity of 50 ppm XG solution in 2 mM buffer, which has a similar profile to that of 50 ppm XG solution in 0.2 mM buffer. One can see that increasing the XG concentration increases both the dynamic viscosity (for the same shear rate) and shear thinning effect, the latter of which is reflected by the decreasing power law index, n, labeled on the plot.

2.2. Methods

Prior to every experiment, the deionized water was emptied from all the three reservoirs of the T-shaped microchannel. An equal volume of 0.2 mM and 2 mM buffer-based XG solutions with the same XG concentration was dispensed into the inlet reservoirs of the two side branches, respectively. The same volume of 0.2 mM buffer was then dispensed into the outlet reservoir of the main branch to balance the liquid height in the inlet reservoirs, removing the hydrostatic pressure-driven flow within the microchannel. The electroosmotic flow of each of the two XG solutions from the inlet to the outlet reservoir was driven by an equal DC electric field through each side branch. This was realized by connecting the platinum electrodes in the inlet reservoirs with a DC power source (Glassman high voltage) in parallel while grounding that in the outlet reservoir. The imposed DC voltages were kept no more than 900 V in all tests, limiting the average electric field to 500 V cm^{-1} over the 1.8 cm channel length. This magnitude of DC electric field has been demonstrated in our earlier paper to cause insignificant Joule heating effects in similar buffer solutions even in a constricted microchannel.[48] To visualize the interfacial behavior between the co-flowing fluids, 2 mM buffer-based solution was mixed with 50 μM neutral rhodamine B dye (Sigma-Aldrich). The dynamic fluid behavior at the T-junction of the microchannel was visualized and recorded using an inverted fluorescent microscope (Nikon Eclipse TE2000U, Nikon instrument) equipped with a CCD camera (Nikon DS-Qi1Mc). The resulting digital images were post-processed using the Nikon imaging software (NIS-Elements AR 2.30).

We revised the critical electric Rayleigh number, Ra$_{e,cr}$, defined in eqn (1) to incorporate the variations of material properties in XG solutions compared to the Newtonian solution (i.e., the solvent of XG solutions in this work). As viewed from Fig. 1(b), the addition of XG polymer increases fluid viscosity, μ, and hence decreases ion diffusivity, D, via the Stokes–Einstein equation,

$$D = \frac{k_B T}{6\pi\mu a} = D_0\left(\frac{\mu_0}{\mu}\right) \tag{2}$$

where k_B is the Boltzmann constant, T is the fluid temperature, a is the radius of ions, D_0 is the diffusivity of ions in the Newtonian solution with μ_0 being its viscosity. Also affected in eqn (1) is the diffusion length, δ, of ions, which can be
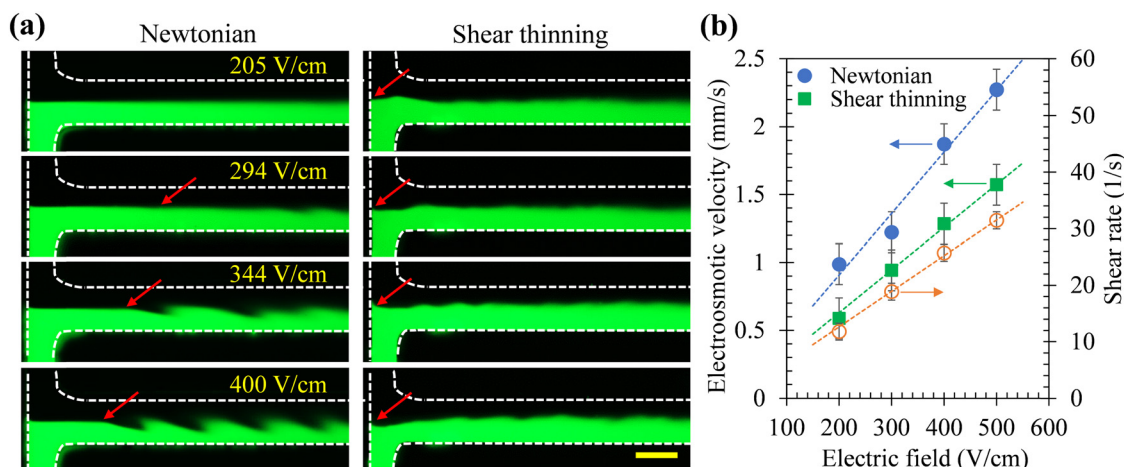

Fig. 2 Electroosmotic flow of 0.2 mM (dark) and 2 mM (dyed) buffer-based solutions at the T-junction under different electric fields: (a) experimental images of the fluid interface in the Newtonian fluid (0 ppm XG, left column) and shear thinning fluid (50 ppm XG, right column). The arrow on each image indicates where the EKI waves first appear under the corresponding electric field. The dashed lines highlight the channel walls, and the scale bar represents 200 μm; (b) experimentally measured electroosmotic velocities of 0.2 mM buffer-based Newtonian (0 ppm XG) and shear thinning (50 ppm XG) fluids and the calculated fluid shear rate in the shear thinning fluid. The dotted lines are linear trendlines fitted to the data points.

estimated from,

$$\delta = 2\sqrt{Dt} = 2\sqrt{D_0\left(\frac{\mu_0}{\mu}\right)\frac{L_{fov}}{U_{eo,0}}\left(\frac{U_{eo,0}}{U_{eo}}\right)}$$
$$= \delta_0\sqrt{\left(\frac{\mu_0}{\mu}\right)\left(\frac{U_{eo,0}}{U_{eo}}\right)} \quad (3)$$

where the time for ion diffusion, t, is estimated from the electroosmotic advection of fluid across the field of view in our experiment with a fixed length of L_{fov}, $U_{eo,0}$ is the electroosmotic velocity in the Newtonian solution, U_{eo} is the electroosmotic velocity in the XG solution, and $\delta_0 = 2\sqrt{D_0 t_0}$ is the ion diffusion length in the Newtonian solution with $t_0 = L_{fov}/U_{eo,0}$. Substituting eqn (2) and (3) into eqn (1) leads to,

$$Ra_{e,cr} = \Gamma\frac{h}{\delta_0}\sqrt{\left(\frac{\mu}{\mu_0}\right)\left(\frac{U_{eo}}{U_{eo,0}}\right)}\frac{\varepsilon E_{th}^2 d^2}{\mu_0 D_0} \quad (4)$$

If we define the critical electric Rayleigh number in the Newtonian solution as $Ra_{e,cr,0}$, the above equation can be further converted into the following form,

$$\frac{Ra_{e,cr}}{Ra_{e,cr,0}} = \left(\frac{\Gamma}{\Gamma_0}\right)\sqrt{\left(\frac{\mu}{\mu_0}\right)\left(\frac{U_{eo}}{U_{eo,0}}\right)}\left(\frac{E_{th}}{E_{th,0}}\right)^2 \quad (5)$$

where $\Gamma_0 = (\gamma_0 - 1)^2/(\gamma_0 + 1)^2$ with γ_0 being the conductivity ratio in the Newtonian case. This ratio of $Ra_{e,cr}$ will be used in the next section to quantify the fluid shear thinning effect on EKI.

3. Results and discussion

3.1. Comparison of EKI in shear thinning and Newtonian fluid flows

Fig. 2(a) shows experimental images of the fluid interface between 0.2 mM and 2 mM buffer-based XG solutions at the T-junction of the microchannel under different DC electric fields. For the case of 0 ppm XG solution, *i.e.*, Newtonian fluid (left column), we observe a similar development of EKI to that
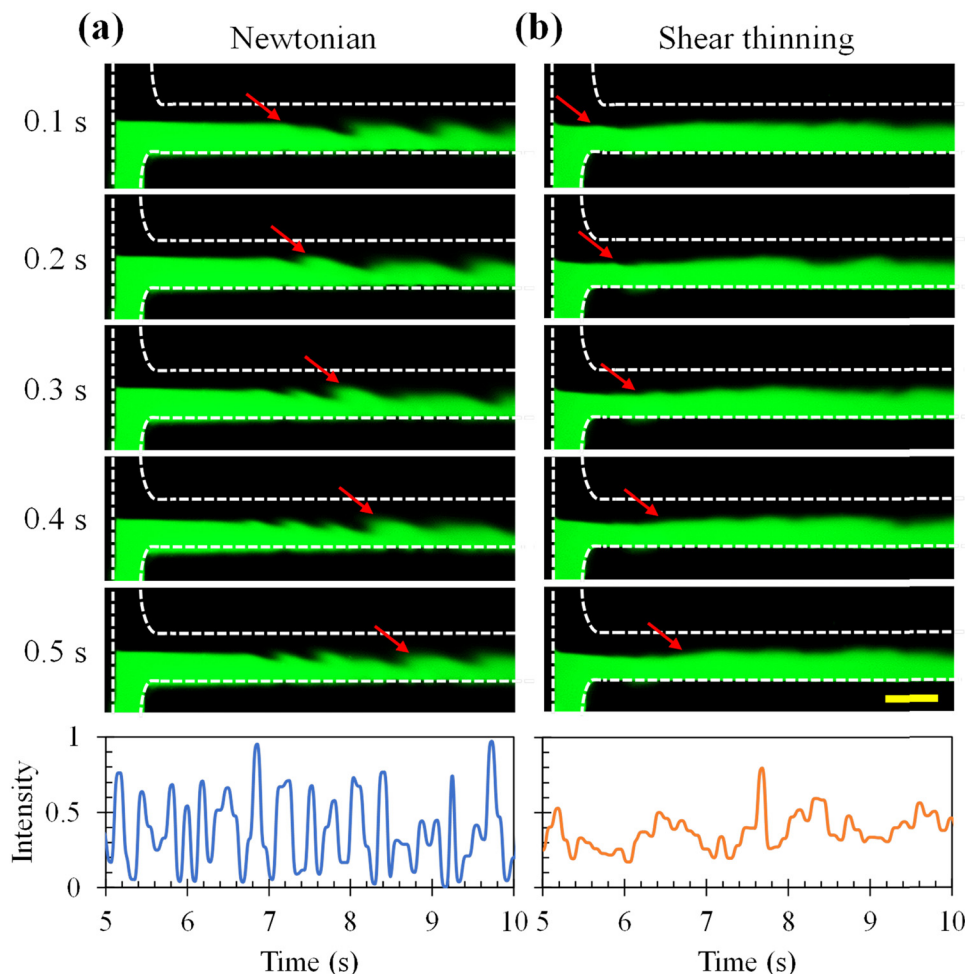

Fig. 3 Comparison of the sequential images (upper panel, time instants labeled to the left of the images) and intensity plots (lower panel, obtained at the fluid interface 600 μm away from the T-junction) of fluorescent dye under 400 V cm^{-1} electric field: (a) Newtonian 0 ppm XG solution; (b) shear thinning 50 ppm XG solution. The arrows on the images track the propagation of EKI waves with time. The dashed lines highlight the channel walls, and the scale bar represents 200 μm.

reported in our recent work.[45] The waves first occur about 0.5 mm away from the T-junction under the threshold electric field of 294 V cm^{-1} (estimated from the total voltage drop of 530 ($\pm$20) V divided by the total length of 1.8 cm between the inlet and outlet reservoirs, consistent with the value obtained in our recent work[45]). They move closer to the T-junction and get stronger in both amplitude and propagation speed with increasing electric field. In contrast, as viewed from the images in Fig. 2(a) for 50 ppm XG solution (right column), the onset of EKI takes place much earlier at the stagnation point of the T-junction, which may be correlated with the local high shear rate and hence large viscosity variations in a shear thinning fluid. Moreover, the threshold electric field, E_{th} = 205 V cm^{-1}, is much smaller in the XG solution than that in the Newtonian fluid.

To compare the critical electric Rayleigh number, $Ra_{e,cr}$, in these two types of fluids, we first estimated the shear rate in the shear thinning fluid *via* $2U_{eo}/h$, where the electroosmotic velocity, U_{eo}, was experimentally measured in 0.2 mM buffer-based 50 ppm XG solution (along with that in 0.2 mM buffer solution) using the electric current monitoring method.[49] As seen from Fig. 2(b), the fluid shear rate is on the order of 10 s^{-1} (specifically 12 s^{-1} under the threshold electric field, E_{th} = 205 V cm^{-1}), which was used to obtain from Fig. 1(b) the fluid viscosity of 50 ppm XG solution. Along with the experimentally measured conductivity ratios in Fig. 1(a), we calculated from eqn (5) the ratio of $Ra_{e,cr}$ as 0.72, indicating a smaller critical electric Rayleigh number in the shear thinning fluid. In other words, our experiment demonstrates the enhancing effect of fluid shear thinning on EKI, which is qualitatively consistent with the prediction of Hamid and Sasmal.[47] However, the EKI waves in the shear thinning fluid flow are visually weaker and less regular than in the Newtonian fluid though they still seem to grow under higher electric fields. This observation contrasts with what Hamid and Sasmal[47] predicted in their numerical simulation, which is probably due to the differences in viscosities and conductivity ratios between the two types of fluids in our experiment.

Fig. 3 compares in two different forms the time evolution of EKI waves between Newtonian 0 ppm XG (a) and shear thinning 50 ppm XG (b) solution flows under the electric field of 400 V cm^{-1}. One form is the sequential images of the fluid interface within a 0.5 s interval, from which we can track the propagation of EKI waves from the onset (see the arrows on the images in Fig. 3) and identify the (largest) amplitude during their propagation. The EKI waves in the Newtonian fluid flow transport faster with a smaller fluctuation of amplitude than in the shear thinning fluid flow. The other form is the intensity plot of the fluid interface at 600 μm away from the T-junction within a 20 s interval (only the data at 5–10 s are shown in the plots), from which we can count the number of spikes and use it to determine the temporal frequency of EKI waves. The intensity plot for the shear thinning fluid flow reveals a larger deviation from a typical periodic wave than that for the Newtonian fluid flow. This phenomenon appears consistent with the observed greater fluctuation in the amplitude of EKI waves in the former.

Fig. 4 compares the experimentally determined properties of EKI waves in Newtonian 0 ppm XG and shear thinning 50 ppm XG solutions under different electric fields. Fig. 4(a) shows the wave speeds in the two fluids, each of which follows an approximately linear relationship with the applied electric field. The EKI waves propagate faster in the Newtonian fluid than in the shear thinning fluid at each electric field, which is correlated with the weaker electroosmotic flow in the latter because of primarily the polymer-addition induced viscosity increase.[50] Fig. 4(b) shows the wave amplitude (relative to the width of the main branch), which also exhibits a linearly increasing trend with the increasing electric field in each of the two fluid flows. The EKI waves have a smaller amplitude in the shear thinning fluid because of perhaps the stronger viscous dampening effect therein. Fig. 4(c) shows the temporal frequency of EKI waves, which increases slowly from around 3 Hz to slightly less than 4 Hz in the Newtonian fluid flow. This trend and range of values is consistent with the convective EKI waves reported in
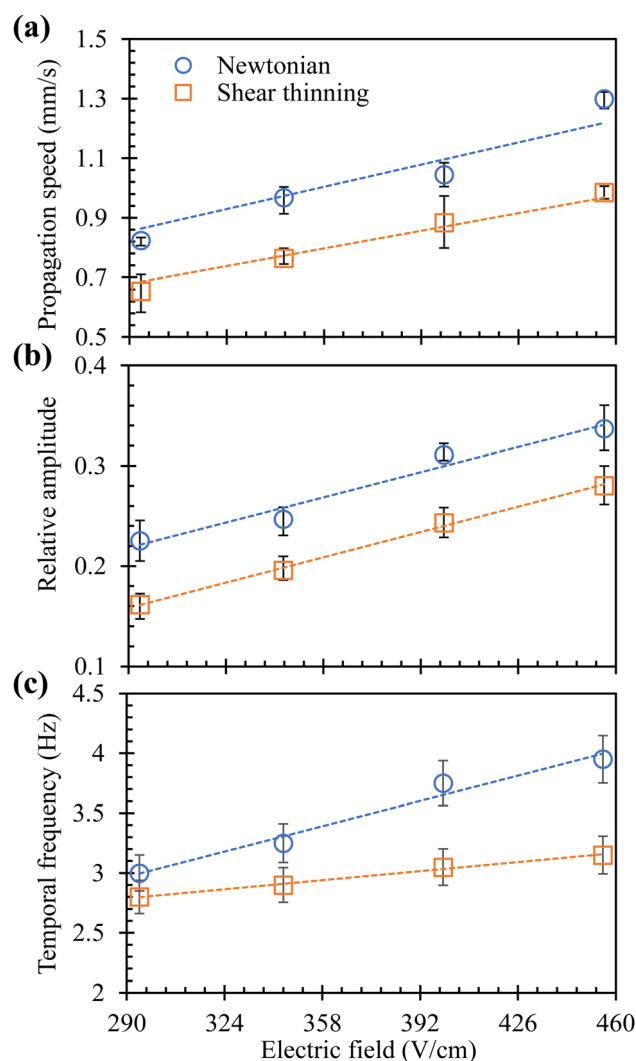

Fig. 4 Comparison of the experimentally determined propagation speed (a), relative amplitude (to the channel width of the main branch) (b), and temporal frequency (c) of EKI waves *vs.* electric field in Newtonian 0 ppm XG and shear thinning 50 ppm XG solutions. The dotted lines are linear trendlines fitted to the data points.
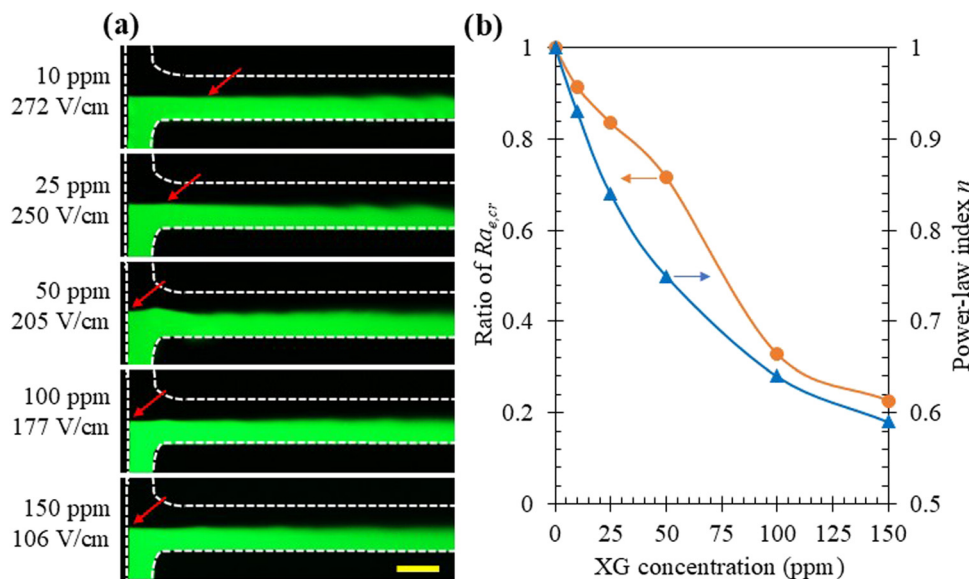
Fig. 5 Effect of XG concentration on the onset of EKI in shear thinning fluid flows: (a) experimental images of the fluid interface between 0.2 mM (dark) and 2 mM (dyed) buffer solutions with various XG concentrations under respective threshold electric fields. The arrow on each image indicates where the EKI waves first appear. The dashed lines highlight the channel walls, and the scale bar represents 200 μm; (b) plots for the ratio of $Ra_{e,cr}$ in eqn (5) and power-law index, n, in Fig. 1(b) vs. XG concentration. The lines are used to guide the eyes only.

both Chen et al.[23] and our recent work.[45] In contrast, the wave frequency in the shear thinning fluid is lower and has only a marginal increase under larger electric fields. Further studies, especially numerical modeling, are needed to understand the observed discrepancies in Fig. 4.

3.2. Effect of polymer concentration

Fig. 5(a) shows the experimental images of EKI waves when the XG concentration varies from 0 to 150 ppm. Two trends are noticed from these images that were each taken under their respective threshold electric fields. The first trend is the continuously decreasing threshold electric field from nearly 300 V cm^{-1} in 0 ppm to approximately 100 V cm^{-1} in 150 ppm XG solution. This trend is believed to be a result of at least three competing factors: (1) the increased shear thinning effect of a higher-XG concentration solution in Fig. 1(b), which promotes EKI as noted in the previous section; (2) the decreased electric conductivity ratio between 2 and 0.2 mM
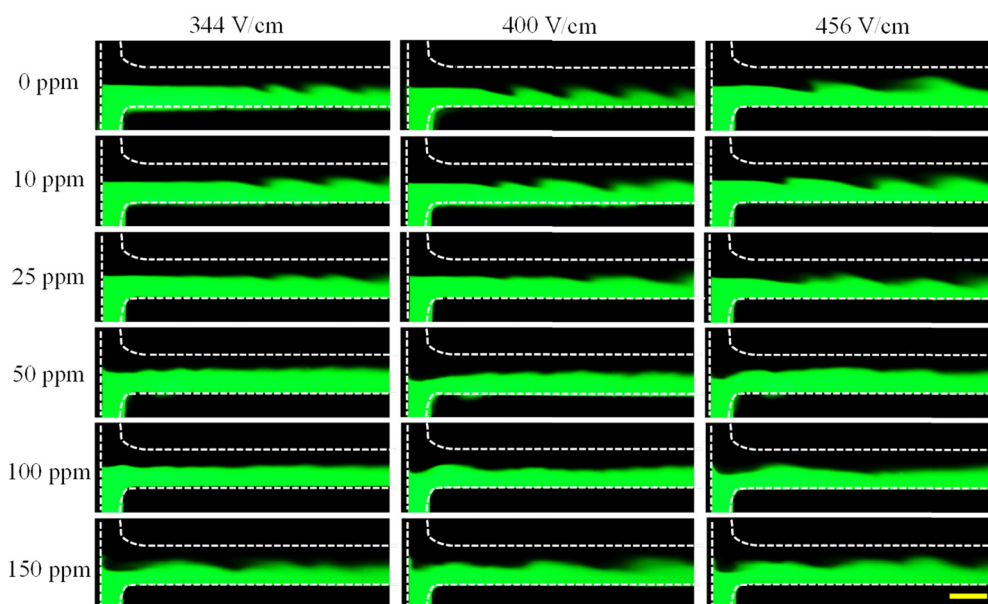

Fig. 6 Comparison of the experimental images of EKI waves in 0.2 mM (dark) and 2 mM (dyed) buffer solutions with various XG concentrations (labeled to the left of the images) under different above-threshold electric fields (labelled on top of the images). The dashed lines highlight the channel walls, and the scale bar represents 200 μm.

buffer solutions with a higher XG concentration in Fig. 1(a), which reduces the electric Rayleigh number in eqn (1) and hence suppresses EKI; (3) the increased fluid viscosity in Fig. 1(b), which also reduces the electric Rayleigh number and in turn EKI. The other trend viewed from the images in Fig. 5(a) is the gradual shifting of the onset location of EKI toward the T-junction as the XG concentration is increased from 0 to 25 ppm. For 50 ppm and higher XG concentrations, EKI waves start appearing at the stagnation point of the T-junction.

To examine how varying the XG concentration changes the critical electric Rayleigh number, $Ra_{e,cr}$, we measured the electroosmotic velocity, U_{eo}, of 2 mM buffer-based XG solutions (with which the fluorescent dye was mixed) for electric fields ranging from 100 to 500 V cm^{-1} like that in Fig. 2(b). The obtained data (to be shown in Fig. 7(a) along with the propagation speed of EKI waves for the electric field of 400 V cm^{-1}) were then used to calculate the fluid shear rates in XG solutions under respective threshold electric fields [labeled on the images in Fig. 5(a)] for reading the fluid viscosities from Fig. 1(b). Fig. 5(b) shows the ratio of $Ra_{e,cr}$ calculated from eqn (5) for the onset of EKI in shear thinning fluids with varying XG concentrations. Also shown in this figure is the power-law index, n, obtained from Fig. 1(b). On one hand, increasing the XG concentration from 0 to 150 ppm decreases the n value from 1 to 0.59 and hence enhances the fluid shear thinning effect. On the other hand, it continuously decreases the ratio of $Ra_{e,cr}$ from 1 to 0.23 and hence promotes the onset of EKI in higher XG concentration solutions. These results together further validate our judge in the preceding section that fluid shear thinning strengthens EKI in microchannel fluid flows with conductivity gradients, consistent with the prediction of Hamid and Sasmal.[47]

Fig. 6 compares the experimental images of EKI waves for XG concentration ranging from 0 to 150 ppm under three above-threshold electric fields. The wave speed, magnitude and frequency all increase with the increasing electric field in every solution like that demonstrated above in Fig. 4. These wave properties, however, do not seem to vary monotonically with the increase of XG concentration under the same electric field. It is obvious from the images in Fig. 6 that the amplitude of EKI waves exhibits a first decrease then increase trend with the increase of XG concentration under each of the three electric fields. The minimum wave amplitude takes place in 50 ppm XG solution. This observation is further supported by the quantitative plots of the propagation speed, relative magnitude and temporary frequency of EKI waves in Fig. 7(a), (b) and (c), respectively. All these wave properties share a similar first decrease then increase profile with respect to the XG concentration under the electric field of 400 V cm^{-1}. Moreover, each of them in 150 ppm XG solution approaches that in the XG-free Newtonian fluid. Such a non-monotonic tend of EKI wave properties with increasing XG concentration is probably due to the associated variations of fluid viscosity/shear thinning effect in Fig. 1(b) and electroosmotic velocity in Fig. 7(a) as well as electric conductivity ratio in Fig. 1(a). A numerical analysis of EKI in shear thinning fluids under our experimental
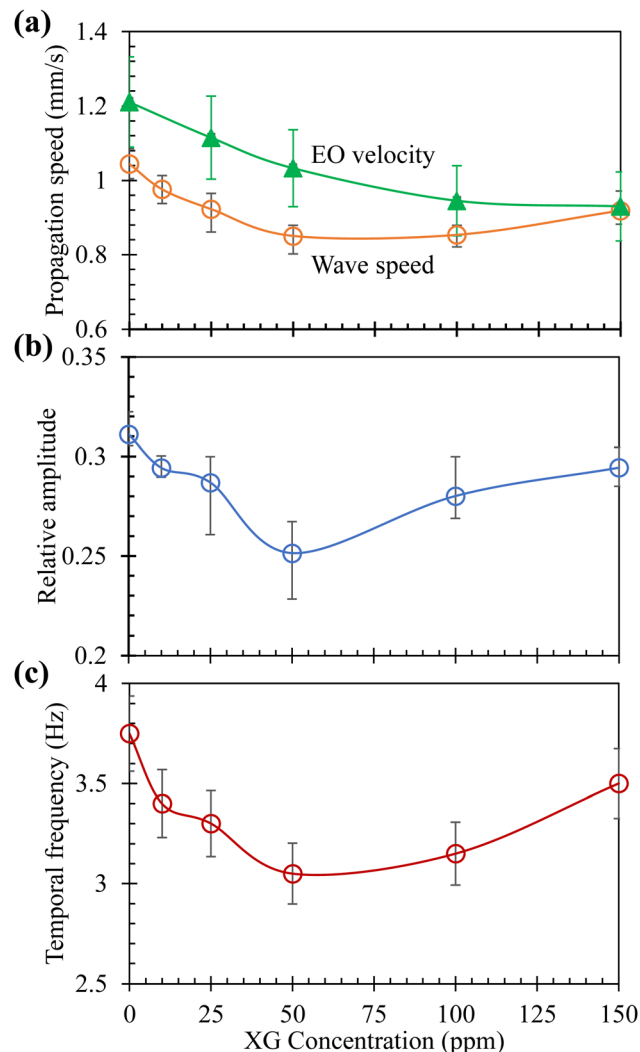

Fig. 7 Effect of XG concentration on the experimentally determined wave properties of EKI under the electric field of 400 V cm^{-1}: (a) propagation speed along with the experimentally measured electroosmotic (EO) velocity of 2 mM buffer-based XG solutions, (b) relative amplitude (to the channel width of the main branch), and (c) temporal frequency. The lines are used to guide the eyes only.

conditions is needed for a better understanding of this phenomenon.

It is to our surprise that the propagation speed of EKI waves does not decrease monotonically with the increase of XG concentration. As seen from Fig. 7(a), the electroosmotic velocity, U_{eo}, decreases with the increasing XG concentration, dissimilar to the first decrease then increase trend of the EKI wave speed. The consequence is that the wave speed nearly catches the electroosmotic velocity of 2 mM buffer-based 150 ppm XG solution. However, as the electroosmotic flow increases in lower-concentration buffer solutions,[51] the wave speed should be still smaller than the average of the electroosmotic velocities of the co-flowing XG solutions. More studies are needed for an improved understanding of the above-mentioned three competing factors (and perhaps other additional factors) that affect the threshold electric field and the

wave properties of EKI in different ways. It is also interesting to test if further increasing the XG concentration beyond 150 ppm will continue enhancing the wave properties and if the wave properties in a shear thinning fluid flow can even surpass those in a Newtonian fluid flow.

4. Conclusions

We have experimentally studied the effects of fluid shear thinning on EKI in electroosmotic fluid flows with conductivity gradients through a T-shaped microchannel. The addition of 50 ppm XG polymer into high- and low-concentration Newtonian buffer solutions is found to significantly lower both the threshold electric field and the critical electric Rayleigh number for the onset of EKI, indicating the enhancing effect of fluid shear thinning. However, the propagation speed, amplitude and frequency of EKI waves are all smaller in the shear thinning XG solution. Increasing the XG concentration from 0 (*i.e.*, Newtonian fluid) to 150 ppm continuously decreases the threshold electric field and the critical electric Rayleigh number. It also continuously shifts the onset location of EKI waves upstream, which remains at the stagnation point of the T-junction for 50 ppm and above XG solutions. In contrast, the wave speed, amplitude and frequency all follow a first decrease then increase trend with increasing XG concentration because of the increased shear thinning, increased viscosity and decreased conductivity ratio along with the influences of other potential factors such as the decreased electroosmotic velocity. This research enhances our understanding of how shear thinning behavior in non-Newtonian fluids affects EKI in microchannel systems. It offers insights for controlling EKI, which is essential for developing microfluidic devices for precision mixing, particle manipulation and biosensing *etc.* In future work we will conduct experiments to investigate the instability in the electroosmotic flow of a Newtonian and a shear thinning fluid with and without conductivity gradients. We hope that our experimental results presented here will stimulate more studies such as the stability analysis of EKI[23] and electroosmotic flow[52] in non-Newtonian fluids.

Author contributions

T. C., M. K. R., S. M. T., C. T. G., M. M. I. and Y. L. performed the experiment; T. C. and M. K. R. conducted the analysis of experimental data; J. B. B., L. F. and X. X. designed and supervised the project; T. C. and M. K. R. wrote the manuscript; X. X. edited the manuscript; all authors commented on the manuscript.

Data availability

The data supporting this article are within the article.

Conflicts of interest

There are no conflicts to declare.

References

1 X. Xuan, *Electrophoresis*, 2019, **40**, 2484–2513.
2 M. Rashidia and A. M. Benneker, *Soft Matter*, 2023, **19**, 3136–3146.
3 B. H. Lapizco-Encinas, *Annu. Rev. Anal. Chem.*, 2024, **17**, 243–264.
4 G. M. Whitesides and A. D. Stroock, *Phys. Today*, 2001, **54**, 42–48.
5 C. Zhao and C. Yang, *Microfluid. Nanofluid.*, 2012, **13**, 179–203.
6 B. Saha, S. Chowdhury, S. Sarkar and P. P. Gopmandal, *Soft Matter*, 2024, **20**, 6458–6489.
7 S. Ghosal, *Annu. Rev. Fluid Mech.*, 2006, **38**, 309–338.
8 S. Ghosal, *Electrophoresis*, 2014, **25**, 214–228.
9 P. Koner, S. Bera and H. Ohshima, *Soft Matter*, 2023, **19**, 983–998.
10 J. R. Melcher and G. I. Taylor, *Annu. Rev. Fluid Mech.*, 1969, **1**, 111–146.
11 H. Lin, *Mech. Res. Commun.*, 2009, **36**, 33–38.
12 R. Bharadwaj and J. G. Santiago, *J. Fluid Mech.*, 2005, **543**, 57–92.
13 A. Ramachandran and J. G. Santiago, *Chem. Rev.*, 2022, **122**, 12904–12976.
14 C. Y. Lim, A. E. Lim and Y. C. Lam, *Anal. Chem.*, 2017, **89**, 9394–9399.
15 M. A. Saucedo-Espinosa and B. H. Lapizco-Encinas, *Biomicrofluidics*, 2016, **10**, 033104.
16 K. Dubey, S. Sanghi, A. Gupta and S. S. Bahga, *J. Fluid Mech.*, 2021, **925**, A14.
17 Y. Song, D. Li and X. Xuan, *Electrophoresis*, 2023, **44**, 910–937.
18 T. Kawamata, M. Yamada, M. Yasuda and M. Seki, *Electrophoresis*, 2008, **29**, 1423–1430.
19 J. Park, S. M. Shin, K. Y. Huh and I. S. Kang, *Phys. Fluids*, 2015, **17**, 118101.
20 C. H. Tai, R. J. Yang, M. Z. Huang, C. W. Liu, C. H. Tsai and L. M. Fu, *Electrophoresis*, 2006, **27**, 4982–4990.
21 J. D. Posner, C. L. Perez and J. G. Santiago, *Proc. Natl. Acad. Sci. U. S. A.*, 2012, **109**, 14353–14356.
22 H. Lin, B. D. Storey, M. H. Oddy, C. Chen and J. G. Santiago, *Phys. Fluids*, 2004, **16**, 1922–1935.
23 C. Chen, H. Lin, S. K. Lele and J. G. Santiago, *J. Fluid Mech.*, 2005, **524**, 263–303.
24 M. H. Oddy and J. G. Santiago, *Phys. Fluids*, 2005, **17**, 064108.
25 H. Lin, B. D. Storey and J. G. Santiago, *J. Fluid Mech.*, 2008, **608**, 43–70.
26 S. M. Shin, I. S. Kang and Y. K. Cho, *J. Micromech. Microeng.*, 2005, **15**, 455–462.

27 D. A. Boy and B. D. Storey, *Phys. Rev. E*, 2007, **76**, 026304.

28 W. J. Luo, *Microfluid. Nanofluid.*, 2009, **6**, 189–202.

29 D. T. Kumar, Y. Zhou, V. Brown, X. Lu, A. Kale, L. Yu and X. Xuan, *Microfluid. Nanofluid.*, 2015, **19**, 43.

30 L. Song, P. Jagdale, L. Yu, Z. Liu, C. Zhang, R. Gao and X. Xuan, *Microfluid. Nanofluid.*, 2018, **22**, 134.

31 G. Navaneetham and J. D. Posner, *J. Fluid Mech.*, 2009, **619**, 331–365.

32 J. D. Posner and J. G. Santiago, *J. Fluid Mech.*, 2006, **555**, 1–42.

33 M. Z. Huang, R. J. Yang, C. H. Tai, C. H. Tsai and L. M. Fu, *Biomed. Microdevices*, 2006, **8**, 309–315.

34 K. Dubey, A. Gupta and S. S. Bahga, *Phys. Fluids*, 2017, **29**, 092007.

35 B. D. Storey, B. S. Tilley, H. Lin and J. G. Santiago, *Phys. Fluids*, 2005, **17**, 018103.

36 L. Song, L. Yu, Y. Zhou, A. R. Antao, R. A. Prabhakaran and X. Xuan, *Sci. Rep.*, 2017, **7**, 46510.

37 L. Song, L. Yu, C. Brumme, R. Shaw, C. Zhang and X. Xuan, *Electrophoresis*, 2021, **42**, 967–974.

38 G. D'Avino, G. Greco and P. L. Maffettone, *Annu. Rev. Fluid Mech.*, 2017, **49**, 341–360.

39 C. A. Browne, A. Shih and S. S. Datta, *Small*, 2020, **16**, 1903944.

40 M. A. Alves, P. J. Oliveira and F. T. Pinho, *Annu. Rev. Fluid Mech.*, 2021, **53**, 509–541.

41 S. Puri and R. M. Thaokar, *Soft Matter*, 2023, **19**, 6945–6957.

42 A. G. Bayram, F. J. Schwarzendahl, H. Löwen and L. Biancofiore, *Soft Matter*, 2023, **19**, 4571–4578.

43 M. K. Raihan, N. Kim, Y. Song and X. Xuan, *Soft Matter*, 2024, **20**, 6059–6067.

44 S. M. Recktenwald, Y. Rashidi, I. Graham, P. E. Arratia, F. Del Giudice and C. Wagner, *Soft Matter*, 2024, **20**, 4950–4963.

45 L. Song, P. P. Jagdale, L. Yu, Z. Liu, D. Li, C. Zhang and X. Xuan, *Phys. Fluids*, 2019, **31**, 082001.

46 C. Sasmal, *Phys. Fluids*, 2022, **34**, 082011.

47 F. Hamid and C. Sasmal, *Phys. Fluids*, 2023, **35**, 013107.

48 S. Sridharan, J. Zhu, G. Hu and X. Xuan, *Electrophoresis*, 2011, **32**, 2274–2281.

49 A. Sze, D. Erickson, L. Ren and D. Li, *J. Colloid Interface Sci.*, 2003, **261**, 402–410.

50 J. Bentor, C. Gabbard, J. Bostwick and X. Xuan, *Langmuir*, 2024, **40**, 20113–20119.

51 B. J. Kirby and E. F. Hasselbrink, *Electrophoresis*, 2004, **25**, 203.

52 G. C. Shit, A. Sengupta and K. Pranab, *J. Fluid Mech.*, 2024, **983**, A13.